Nano Research

Open Access

Research Article

# Potential-induced bis-axial coordination in Ir-N-C single-atom catalyst delivers selective C–N coupling for efficient methane amination

Wenying Li, Zeyu Wang, Jun Li, and Hai Xiao ✉

*Department of Chemistry, Tsinghua University, Beijing 100084, China*

Cite this article: *Nano Research*, **2026**, *19*, 94908484. https://doi.org/10.26599/NR.2026.94908484

**ABSTRACT:** Direct electrochemical functionalization of methane remains fundamentally limited by the difficulty of stabilizing reactive $CH_x$ intermediates while suppressing overoxidation and competing side reactions. Using grand-canonical ensemble density functional theory (GCE-DFT), we reveal how an applied anodic potential induces evolution of the axial coordination environment on a graphene-supported $IrN_4$ single-atom catalyst to enable selective methane amination. Constant-potential GCE-DFT calculations show that $IrN_4$ evolves into a bis-axial $*CH_2$–$*NH_2$ resting state that dominates over a broad potential–pH window. This potential-induced configuration offers dual advantages: It excludes oxygenated ligands to suppress the oxygen evolution reaction and stabilizes a reactive, electrophilic surface $*CH_2$ carbene. Electronic structure analyses identify minimized Pauli repulsion and cooperative σ–π interactions as the key factors governing this preferential axial coordination. Kinetic analyses further demonstrate that $*CH_2$ in this bis-axial $*CH_2$–$*NH_2$ motif acts as a chemoselective electrophile that delivers low-barrier, concerted C–N coupling with solution-phase $NH_3$, outperforming competing C–C and C–O coupling pathways. These findings establish potential-induced axial coordination as a powerful design principle for directing single-atom catalysis and provide a mechanistic foundation for selective methane-to-amine conversion.

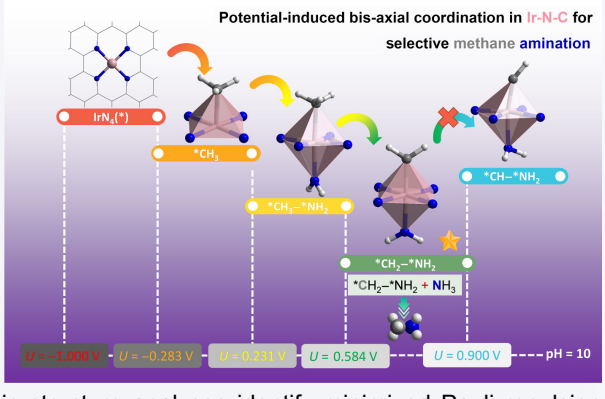


**KEYWORDS:** grand-canonical ensemble density functional theory (GCE-DFT), single-atom catalysis, bis-axial coordination, electrocatalytic methane amination, C–N coupling

## 1 Introduction

Methane ($CH_4$), the primary component of natural gas, is an abundant carbon resource, yet its chemical inertness hinders its efficient valorization [1]. The exceptionally strong C–H bond and nonpolar nature of $CH_4$ make its selective activation under mild conditions a grand challenge [2–4]. Conventional methane upgrading relies on energy-intensive processes such as steam reforming and methanol-mediated amination, which typically suffer from low carbon efficiency and substantial $CO_2$ emissions [5–7]. Thus, developing low-temperature and renewable-electricity-driven strategies for direct $CH_4$ functionalization has emerged as a major objective in sustainable catalysis and carbon management [8–10].

Recent advances in electrochemical methane activation have begun to reshape this landscape [8, 11–14]. Experimental studies have shown that anodic potentials can partially activate $CH_4$ to surface-bound $CH_x$ intermediates ($x$ = 1–3) without driving extensive overoxidation to $CO_2$ [15–17]. Even more strikingly, electrochemical C–N coupling has recently been demonstrated for the direct functionalization of $CH_4$ with $NH_3$ to form methylamine under anodic conditions [13]. In this pioneering experimental work, methane was activated electrochemically without undergoing complete oxidation, enabling C–N bond formation at the electrode–electrolyte interface. The study showed that methylamine could be produced with appreciable efficiency under ambient conditions, demonstrating the feasibility of coupling electrochemical C–H activation with nitrogen functionalization. Notably, this work highlighted that both the reaction efficiency and selectivity are highly sensitive to the applied potential and the

**Received:** December 31, 2025; **Revised:** January 20, 2026
**Accepted:** January 21, 2026

✉Address correspondence to haixiao@tsinghua.edu.cn

nature of the catalytic interface, reflecting the delicate interplay between $CH_4$ activation, intermediate stabilization, and competing side reactions. Despite this experimental breakthrough, the underlying reaction mechanism remains poorly understood. The identification of transient $CH_x$ and $NH_y$ intermediates under electrochemical conditions is experimentally challenging, and the heterogeneity of commonly employed oxide catalysts obscures the precise nature of the active sites [18–20].

Metal single-atom catalysts (SACs) anchored on nitrogen-doped carbon (M-N-C) offer an ideal platform for mechanistic elucidation and thus rational catalyst design, owing to their well-defined active sites for establishing distinct structure–activity correlations [21–29]. Among these, the Ir-N-C SAC featuring an $IrN_4$ moiety is of particular interest for selective activation of $CH_4$ [30, 31]. As a 5d transition metal, Ir possesses spatially extended and energetically flexible d orbitals capable of forming balanced σ-donation and π-backdonation interactions with carbon intermediates. These features are particularly important for stabilizing the $CH_2$ intermediate, which is widely recognized as a decisive branching point in methane functionalization. Moreover, $IrN_4$ displays a relatively weak oxygen affinity compared to $NiN_4$ or $FeN_4$, which may suppress competing oxygen evolution reaction (OER) and mitigate deep dehydrogenation to carbon deposits, a common catalyst deactivation mode in methane electrooxidation [32, 33].

Nevertheless, the catalytic capability of $IrN_4$ to drive electrochemical $CH_4$ activation and subsequent C–N coupling has not yet been explored. Fundamental questions must be addressed to rationalize its catalytic potential. First, how does the applied potential reshape the free-energy landscape of $CH_4$ activation on an $IrN_4$ site? Second, in a reactive environment containing $H_2O$, $NH_3$, and $CH_4$, can the axial coordination of Ir preferentially exclude oxygen-containing species for OER while stabilizing active intermediates such as $CH_2$ or NH against deeper dehydrogenation, and what is the physical origin of this selectivity? Finally, can such resting state $CH_2$/NH species effectively deliver high-activity and high-selectivity C–N coupling, and what is the fundamental driving force governing this process?

To address these questions, we performed potential-dependent grand-canonical ensemble density functional theory (GCE-DFT) calculations [34–37] to delineate the elementary steps of methane amination on an $IrN_4$ single-atom site. We reveal that at representative anodic potentials (e.g., 1.2 V vs. reversible hydrogen electrode (RHE), pH = 10), the $IrN_4$ active site undergoes a distinct coordination evolution: It preferentially activates $CH_4$ to a $*CH_2$ intermediate while simultaneously capturing $NH_3$ at the trans-axial position as $*NH_2$. This leads to a robust bis-axial $CH_2$–Ir–$NH_2$ resting state that persists over a wide potential window. Electronic structure analyses further elucidate that this configuration is stabilized by a unique interplay of minimized Pauli repulsion and σ–π synergism. Finally, kinetic studies demonstrate that $*CH_2$ in this bis-axial motif displays exceptional reactivity and selectivity toward solution-phase $NH_3$. The reaction proceeds through a concerted hydrogen transfer and C–N coupling mechanism, which effectively suppresses competing C–C or C–O bond formation and ultimately yields methylamine. Overall, our results provide the first atomic-scale evidence that a potential-induced bis-axial $IrN_4$ motif can mediate a complete, highly selective electrochemical methane-to-methylamine cycle. These insights not only clarify the potential-dependent reaction landscape but also offer guiding principles for the rational design of next-generation electrocatalysts for direct methane-to-amines conversion.

## 2 Computational methodology

Spin-polarized periodic density functional theory (DFT) calculations were performed using the Vienna *ab initio* simulation package (VASP, version 6.3.2) [38–40]. Electronic exchange–correlation effects were treated within the generalized gradient approximation (GGA) using the Perdew–Burke–Ernzerhof (PBE) functional [41], while core–valence interactions were described by the projector augmented wave (PAW) method [42, 43]. The plane-wave basis set with a kinetic energy cutoff of 500 eV was adopted, and electronic occupancies were smeared using the Gaussian scheme with a width of 0.05 eV.

The Ir-N-C SAC was modeled using a (6 × 6) graphene supercell separated by a 30 Å vacuum layer to eliminate spurious periodic interactions. The Brillouin zone was sampled with a Γ-centered 3 × 3 × 1 Monkhorst–Pack k-point grid [44]. The electronic self-consistent field (SCF) calculations were converged to within $1 \times 10^{-5}$ eV for energy, and the ionic relaxations and transition state (TS) optimizations were converged to within 0.03 eV/Å for forces. TSs were located using the improved dimer method and confirmed by vibrational frequency analysis, ensuring the presence of a single imaginary frequency mode [45, 46].

Electrochemical interfaces were modeled using the GCE-DFT framework combined with a nonlinear, spatially nonlocal implicit electrolyte model as implemented in VASPsol++ [34–37, 47]. The electrode potential ($U$) served as the control variable; the total number of electrons was dynamically optimized to align the Fermi level with $U$, and charge neutrality was maintained by the implicit electrolyte model [29, 37, 48–50]. Full structural optimizations within the GCE-DFT framework were performed to explicitly evaluate the $U$-dependent grand-canonical free energy ($\Omega$).

Periodic energy decomposition analysis (pEDA) was performed using the BAND module of the Amsterdam Modeling Suite (AMS2022.103) [51–54]. These calculations employed the PBE functional and a Slater-type triple-ζ polarized (TZP) basis set for all atoms without the frozen core approximation. Scalar relativistic effects were taken into account using the zeroth-order regular approximation (ZORA) implemented in BAND.

## 3 Results and discussion

### 3.1 Potential-induced evolution of axial coordination in Ir-N-C SAC

To decipher the electrochemical methane amination mechanism on $IrN_4$ sites of Ir-N-C SAC, we performed constant-potential calculations within the GCE-DFT framework to systematically investigate the potential- and pH-dependent structural evolution of the $IrN_4$ active center under *operando* conditions. We focused on a representative anodic environment with $U$ = 1.20 V vs. RHE (corresponding to 0.61 V vs. standard hydrogen electrode (SHE) at pH = 10) and a 0.1 M aqueous ammonia buffer. This $U$ value was chosen to maximize the driving force for C–H activation while remaining below the onset potential of the competing OER (1.23 V vs. RHE). By explicitly modeling proton-coupled electron transfer (PCET) steps in successive dehydrogenation of $CH_4$, $NH_3$, and $H_2O$ on the $IrN_4$ site, we systematically mapped the competitive

adsorption and dehydrogenation landscapes for both mono-axial and bis-axial coordination motifs on the Ir center under this anodic condition.

Figure 1(a) outlines the $\Omega$ landscapes of stepwise axial coordination evolution on the $IrN_4$ site at $U$ = 1.20 V vs. RHE and pH = 10. Starting from the pristine surface, the Ir center faces competitive adsorption from solvent water, ammonia, and methane. Our GCE-DFT results reveal a distinct chemoselectivity: The oxidative activation of $CH_4$ to a mono-axially coordinated $*CH_3$ species ($* + CH_4 + OH^- - e^- \rightarrow *CH_3 + H_2O$) is thermodynamically favorable, outcompeting both $*NH_2$ and *OH formation. This initial C–H activation triggers a transition to a bis-axial coordination configuration. As dehydrogenation proceeds, the vacant axial site trans to the $*CH_3$ species captures an ammonia molecule, evolving into a bis-axial coordination motif, denoted as $*CH_3$–$*NH_2$, via an exothermic PCET step ($*CH_3 + NH_3 + OH^- - e^- \rightarrow *CH_3$–$*NH_2 + H_2O$). Subsequently, the system undergoes thermodynamically downhill, preferential oxidation of $*CH_3$ species to form $*CH_2$–$*NH_2$ ($*CH_3$–$*NH_2 + OH^- - e^- \rightarrow *CH_2$–$*NH_2 + H_2O$). Crucially, the axial coordination evolution stabilizes at this stage. The subsequent PCET step from $*CH_2$–$*NH_2$ to *CH–$*NH_2$ ($*CH_2$–$*NH_2 + OH^- - e^- \rightarrow *CH$–$*NH_2 + H_2O$) becomes endothermic, indicating that the applied potential of 1.20 V vs. RHE is insufficient to drive further C–H bond cleavage. Consequently, the bis-axial $*CH_2$–$*NH_2$ configuration emerges as the thermodynamic sink, i.e., the resting state under the applied electrochemical conditions.

To rigorously delineate the stability domain of this active motif, we constructed a surface Pourbaix diagram (Fig. 1(c)) spanning pH values from 7.0 to 14.0 and electrode potentials from −1.0 to +1.0 V vs. SHE. This diagram confirms that at pH = 10, the $*CH_2$–$*NH_2$ configuration is the thermodynamically dominant surface phase within a wide potential window of 0.584–0.900 V vs. SHE. The persistence of this potential-induced bis-axial $CH_2$–$IrN_4$–$NH_2$ motif provides two critical advantages: (i) The saturation of both axial sites by $*CH_2$ and $*NH_2$ effectively blocks the adsorption of *OH/*O species, thereby suppressing the competing OER; (ii) the Ir center maintains the carbon species in a reactive $*CH_2$ state, laying the foundation for subsequent C–N coupling between $*CH_2$ and molecular $NH_3$ to yield the target methylamine ($CH_3NH_2$).

### 3.2 Electronic origins of selective axial ligand coordination

To rationalize the thermodynamic preference for $*CH_3$ as the primary axial ligand and $*NH_2$ as the secondary ligand at $U$ = 1.20 V vs. RHE and pH = 10, we scrutinized the underlying electronic descriptors governing the potential-dependent adsorbate–$IrN_4$ interactions. Projected density of states (PDOS, Fig. 2(a)) and integrated crystal orbital Hamilton population (ICOHP, Table S1 in the Electronic Supplementary Material (ESM)) analyses reveal that the Ir–A bond (A = C/N/O of $CH_3$/$NH_2$/OH group) is predominantly driven by σ-type interactions between the Ir $5d_{z^2}$ orbital and the adsorbate $2p_z$ orbital.

Thus, the weakest binding affinity of *OH can be traced to a profound frontier orbital energy mismatch. That is, the O $2p_z$ states, stabilized by a high effective nuclear charge and electronegativity, reside at energies significantly lower than those of N or C $2p_z$ states and Ir $5d_{z^2}$ states (Figs. 2(a) and 2(b)). This energy misalignment not only attenuates the productive orbital overlap of O $2p_z$ with Ir $5d_{z^2}$ (Fig. 2(b)) manifold but also pushes the $5d_{z^2}$ states toward the antibonding region (Fig. 2(c)). Consequently, the Ir–O bond exhibits diminished covalency and pronounced ionic polarization. This is corroborated by the differential charge density of the HO–$IrN_4$ configuration (Fig. 3(a)), which shows significant electron accumulation on O and electron depletion in the Ir–O bonding region. Bader charge analysis (Fig. 3) further confirms this trend: The positive charge on Ir increases monotonically from the bare site (+0.83 |e|) to $*CH_3$ (+1.12 |e|), $*NH_2$ (+1.29 |e|), and *OH (+1.38 |e|). This identifies *OH as a potent electron-withdrawing ligand that induces a charge-starved Ir center, thereby rendering axial oxygen coordination thermodynamically unfavorable compared to the more covalent Ir–C and Ir–N linkages.

Nevertheless, the competition between $*NH_2$ and $*CH_3$ is governed by a subtle interplay of forces. Although PDOS analysis

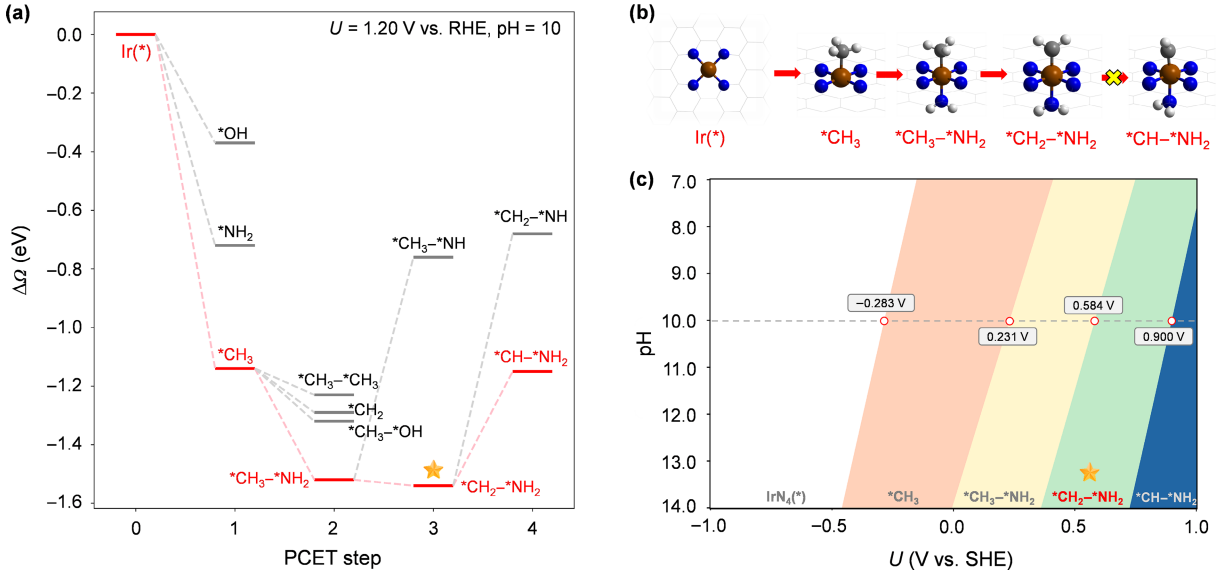


**Figure 1** (a) $\Omega$ profile and (b) the most stable configuration for each PCET step of the potential-induced adsorption and dehydrogenation of $CH_x$ ($x$ = 4, 3, 2, 1, 0), $NH_y$ ($y$ = 3, 2, 1, 0), and $OH_z$ ($z$ = 2, 1, 0) species on the $IrN_4$ site (denoted as *) at $U$ = 1.20 V vs. RHE and pH = 10. (c) Surface Pourbaix diagram of $IrN_4$-derived motifs with mono- and bis-axial $CH_x$/$NH_y$/$OH_z$ coordination.

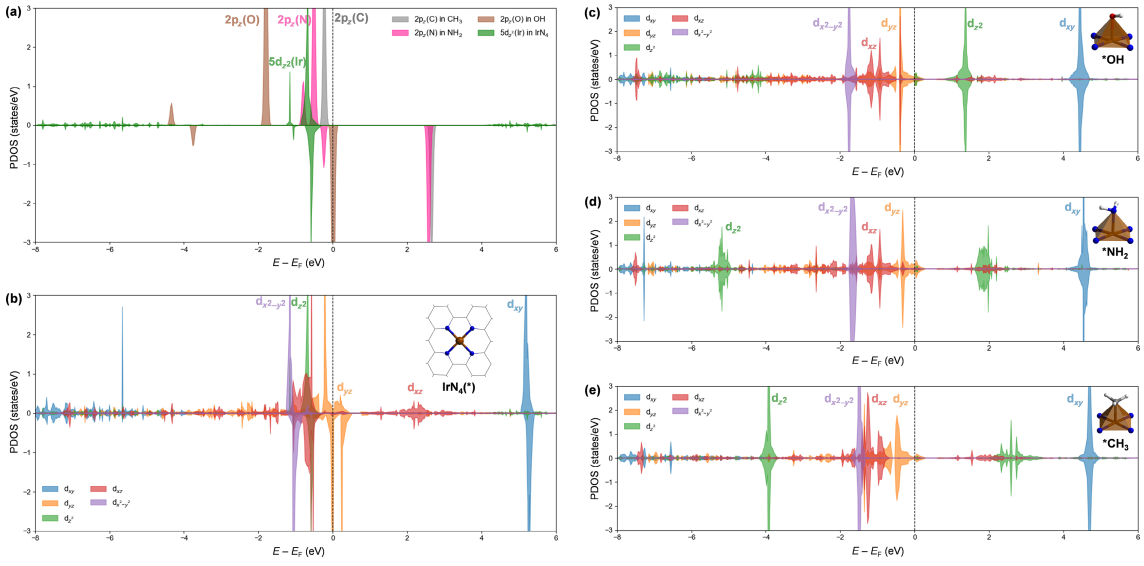


**Figure 2** PDOS of (a) the 2p$_z$ orbitals of C, N, and O atoms in corresponding $CH_3$, $NH_2$, and OH radicals, along with the 5d$_{z^2}$ orbital of Ir in pristine $IrN_4$ moiety. Individual 5d orbitals of Ir for (b) pristine $IrN_4$ and the mono-axially adsorbed (c) *OH, (d) *$NH_2$, and (e) *$CH_3$ structures.

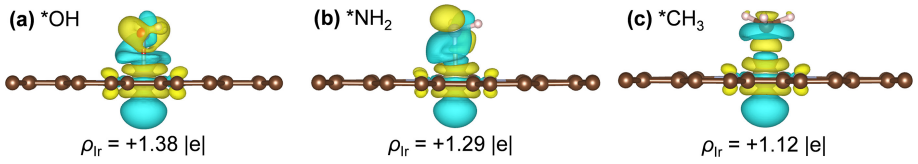


**Figure 3** Charge density difference plots and Bader charges of Ir for the mono-axially adsorbed (a) *OH, (b) *$NH_2$, and (c) *$CH_3$ species on $IrN_4$. Yellow and cyan regions represent electron accumulation and depletion, respectively.

indicates better energy alignment between N 2p$_z$ and Ir 5d$_{z^2}$ (Figs. 2(a) and 2(b)) and ICOHP analysis (Table S1 in the ESM) suggests stronger Ir–N bonding (a more negative ICOHP value for the Ir–N interaction) with a shorter Ir–N bond length, *$NH_2$ is thermodynamically less favored than *$CH_3$ as the first axial ligand (Fig. 1(a)). To reconcile this apparent contradiction, we employed the BAND-based pEDA scheme to dissect the total interaction energy into its underlying physical contributions. As listed in Table 1, the interaction energy ($E_{int}$) is partitioned into Pauli repulsion ($E_{Pauli}$), electrostatic interaction ($E_{elstat}$), and orbital interaction ($E_{orb}$). The orbital interaction component is further resolved into kinetic ($T_{orb}$), polarization-induced orbital electrostatic ($Elst_{orb}$), and exchange–correlation ($XC_{orb}$) contributions.

The pEDA results reveal that *$NH_2$ incurs substantially larger $E_{Pauli}$ and polarization penalties ($Elst_{orb}$) than *$CH_3$. This is directly attributed to the presence of lone pair on the N atom, which imposes severe short-range repulsion upon approaching the Ir center, thereby offsetting the gains from favorable orbital energy alignment, as reflected by the most negative $T_{orb}$ for *$NH_2$ (Table 1) and the strong 5d$_{z^2}$(Ir)–2p$_z$(N) overlap inferred from PDOS analysis (Fig. 2(d)). In contrast, *$CH_3$ achieves a more favorable electronic balance. It benefits from moderate orbital overlap (Fig. 2(e)) and substantial charge transfer, as evidenced by the differential charge density map (Fig. 3(c)), while simultaneously minimizing Pauli repulsion due to its more diffuse σ-bonding electron distribution. This balanced interplay between σ donation and mitigated steric–electronic repulsion enables the formation of a robust covalent Ir–C bond. Thus, the thermodynamic preference for initial axial ligand selectivity is governed by both the intrinsic bonding and the minimization of Pauli repulsion, favoring the formation of mono-axial *$CH_3$ in the initial PCET step.

Following the formation of the mono-axial *$CH_3$ motif, we examined the stability of subsequent bis-axial coordination, including the homomeric *$CH_3$–*$CH_3$, the heteromeric *$CH_3$–*OH and *$CH_3$–*$NH_2$ configurations. As shown in Fig. 1(a), the symmetric *$CH_3$–*$CH_3$ configuration is the least stable. PDOS analysis (Fig. 4(a)) reveals that coordination of the first *$CH_3$ ligand substantially lowers the energy of the Ir 5d$_{z^2}$ orbital (Fig. 2(e)) through effective σ bonding. Consequently, a second $CH_3$ ligand faces a significantly depleted Ir 5d manifold, leading to competitive orbital overlaps of the axial σ channel that weakens the Ir–C interaction. Tables S1 and S2 in the ESM show that ICOHP drops from −3.51 eV in the mono-axial configuration to −2.51 eV in the bis-axial dimethyl structure. Correspondingly, the Ir–C bond length increases from 2.05 to 2.18 Å. The *$CH_3$–*OH configuration fares better due to a distinct push–pull electronic effect. The electron-withdrawing *OH ligand alleviates electron–electron repulsion at the Ir site, thereby reinforcing the trans-axial Ir–C bond (a more negative ICOHP value of −3.18 eV in Table S2 in the ESM). However, the weak intrinsic stability of the Ir–O bond (an ICOHP value of −2.35 eV in Table S2 in the ESM) limits the overall favorability of this state.

The global thermodynamic minimum among all bis-axial motifs is achieved by the heteromeric *$CH_3$–*$NH_2$ configuration, which exhibits exceptional electronic cooperativity. Beyond the primary σ interaction between Ir 5d$_{z^2}$ and N 2p$_z$ orbitals (Fig. 4(c)), ICOHP and PDOS analyses (Table S2 in the ESM and Fig. 4(d)) reveal a secondary stabilizing contribution, i.e., a symmetry-allowed π-bonding between Ir 5d$_{yz}$ and N 2p$_y$ orbitals. This σ–π synergism, complemented by moderate 6s(Ir) ← 2s(N) back-donation, constructs a robust bonding framework that stabilizes the bis-axial coordination in $CH_3$–$IrN_4$–$NH_2$.

Finally, we note that the bis-axial *$CH_3$–*$NH_2$ coordination is

**Table 1** pEDA (in kcal/mol) for the interaction between the graphene-supported $IrN_4$ single-atom catalyst (Frag. 1, denoted as Ir-N-C) and the mono-axially adsorbed species (Frag. 2, $CH_3$/$NH_2$/OH)

| Structure | Frag. 1 | Frag. 2 | $E_{int}$ | $E_{Pauli}$ | $E_{elstat}$ | $E_{orb}$ | | |
|---|---|---|---|---|---|---|---|---|
| | | | | | | $T_{orb}$ | $Elst_{orb}$ | $XC_{orb}$ |
| *$CH_3$ | Ir-N-C | $CH_3$ | −51.75 | 230.30 | −140.23 | −1380.77 | 1142.72 | 96.51 |
| *$NH_2$ | Ir-N-C | $NH_2$ | −39.35 | 291.15 | −171.62 | −1716.45 | 1435.78 | 121.79 |
| *OH | Ir-N-C | OH | −43.05 | 266.22 | −134.92 | −1619.61 | 1335.71 | 109.55 |

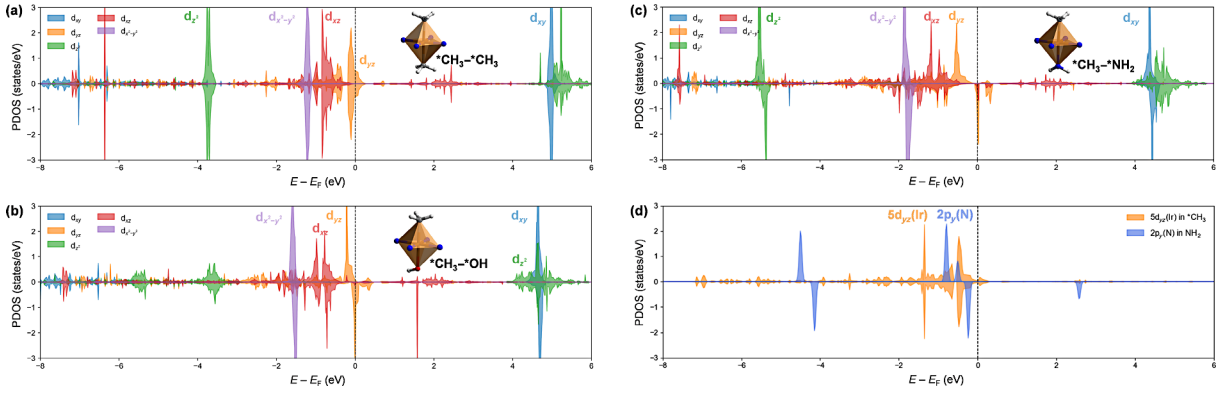


**Figure 4** PDOS of individual 5d orbitals of Ir for the bis-axially adsorbed (a) *$CH_3$–*$CH_3$, (b) *$CH_3$–*OH, and (c) *$CH_3$–*$NH_2$ structures. (d) PDOS of the $2p_y$ orbitals of N atom in $NH_2$ radical, along with the $5d_{yz}$ orbital of Ir in mono-axially adsorbed *$CH_3$ structure.

strongly preferred over the mono-axial alternative by two dehydrogenation steps, i.e., the *$CH_2$ configuration, as shown in Fig. 1(a). The evolution to a *pseudo*-octahedral coordination allows the Ir center to adopt an effective $d^2sp^3$-like hybridization scheme, which maximizes orbital overlap and electronic delocalization between the Ir 5d orbitals and the axial ligands. Subsequent PCET step selectively drives dehydrogenation of the carbon moiety within this stable bis-axial framework to yield the *$CH_2$–*$NH_2$ resting state (Fig. 1(a)). Pourbaix analysis further confirms that *$CH_2$–*$NH_2$ exhibits remarkable electrochemical stability across a broad range of potentials and pH values (Fig. 1(c)). Thus, *$CH_2$–*$NH_2$ emerges as a pivotal precursor that prevents deep dehydrogenation to *CH and locks the reactive *$CH_2$ for subsequent C–N coupling.

### 3.3 Bis-axial *$CH_2$–*$NH_2$ motif delivers kinetically facile and selective C–N coupling

Having identified the bis-axial *$CH_2$–*$NH_2$ motif as the resting state at $U$ = 1.20 V and pH = 10, we proceeded to evaluate its kinetic competence toward product formation. Specifically, we examined the competitive coupling of the activated *$CH_2$–*$NH_2$ moiety with solution-phase $CH_4$, $NH_3$, and $H_2O$ to form C–C, C–N, and C–O bonds, respectively. Given that the axial *$NH_2$ ligand is coordinatively saturated and resistant to further oxidative dehydrogenation, the coupling reactivity is exclusively localized at the electrophilic methylene carbon center.

Our calculated grand-canonical free energy profiles (Fig. 5(a)) reveal that all three coupling pathways proceed via a concerted mechanism. In this elementary step, the incoming nucleophile $AH_n$ ($CH_4$/$NH_3$/$OH_2$) attacks the surface *$CH_2$ species to form a C–A bond, triggering a simultaneous hydrogen transfer from the nucleophile to the methylene carbon. The corresponding TSs are characterized by a distinctive triangular [A–H–C] geometry, where the transferring H bridges the incoming heteroatom and the methylene carbon, leading directly to the formation of the methylated product (e.g., $CH_3NH_2$).

Energetically, the C–N coupling pathway is kinetically dominant, exhibiting the lowest activation barrier of only 0.58 eV. This is substantially lower than the barriers calculated for C–C coupling (0.83 eV) and C–O coupling (0.97 eV). The origin of this kinetic preference lies in the nucleophilicity of the coupling partner relative to the electrophilicity of the surface carbene. The *$CH_2$ moiety possesses an empty 2p orbital and thus behaves as a strong Lewis acid. $NH_3$, with its accessible high-energy lone pair, acts as an ideal Lewis base. This donor–acceptor matching enables strong interactions, significant charge transfer, and favorable orbital overlap in the TS. Structurally, this strong interaction is manifested by a contracted C–N distance of 1.53 Å in the TS, indicating pronounced covalent bond development. After methylamine formation, the Ir center evolves into a mono-axially coordinated *$NH_2$ species, as illustrated in Fig. S1 in the ESM. Through a sequence of consecutive exothermic PCET steps (*$NH_2$ → *$CH_3$–*$NH_2$ → *$CH_2$–*$NH_2$), the catalyst recovers the thermodynamically stable bis-axial *$CH_2$–*$NH_2$ configuration, thereby completing the catalytic cycle.

To quantitatively deconvolute these kinetic trends, we applied the activation strain model (ASM) based energy decomposition analysis [55]. As illustrated in Fig. 5(b), the activation barrier is decomposed into the strain energy required to deform the reactants and the interaction energy between them. Our analysis reveals that the kinetic preference for C–N coupling is primarily driven by a superior interaction energy. The strong orbital mixing between the lone pair of N and the 2p of carbene stabilizes the TS far more effectively than in the competing cases.

In stark contrast, C–O coupling is disfavored by the high electronegativity of oxygen, which deeply stabilizes the lone pairs of water, rendering reduced nucleophilicity that results in poor energetic matching with the electrophilic carbon center and a weakly stabilized transition state. The C–C coupling pathway with $CH_4$ also suffers from a higher kinetic barrier, as methane lacks accessible lone pairs and is characterized by a saturated σ-bonding

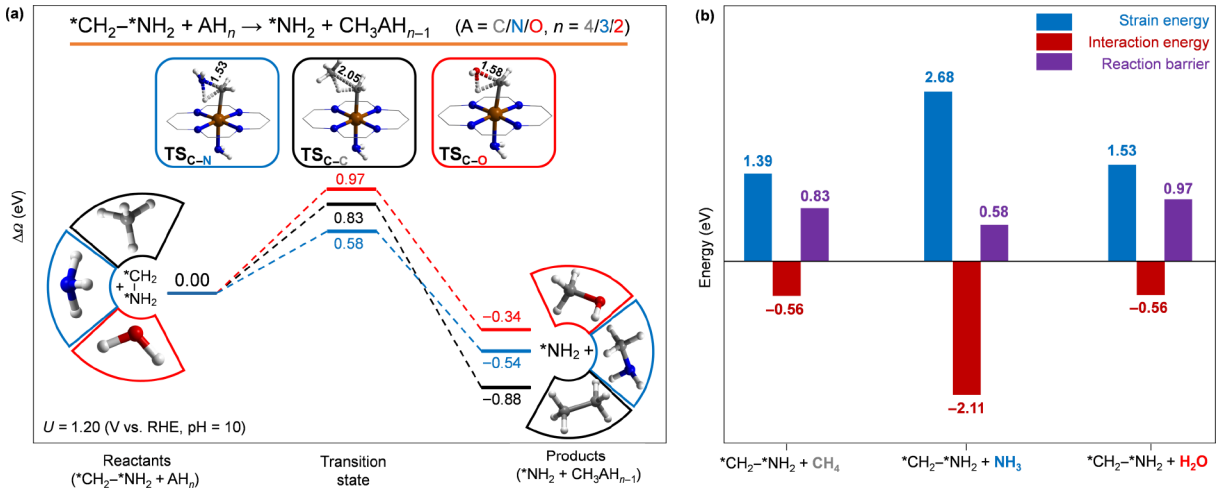


**Figure 5** (a) Ω profiles and relevant key fragments of structures for the coupling of the bis-axially adsorbed $*CH_2$–$*NH_2$ with molecular $CH_4$, $NH_3$, and $H_2O$ at $U$ = 1.20 V vs. RHE (pH = 10). (b) ASM analysis for the coupling of the bis-axially adsorbed $*CH_2$–$*NH_2$ with molecular $CH_4$, $NH_3$, and $H_2O$ at $U$ = 1.20 V vs. RHE (pH = 10).

framework. Consequently, the C–C coupling between $CH_4$ and $*CH_2$ must proceed through a sterically demanding C–H bond activation, which incurs substantial Pauli repulsion and lacks the stabilizing donor–acceptor interactions present in C–N coupling.

Collectively, these mechanistic insights demonstrate that the $IrN_4$ site operates as a chemoselective electrophile. By locking the carbon intermediate in the reactive $*CH_2$ state via bis-axial coordination, the catalyst kinetically discriminates against C–C and C–O coupling with weak nucleophiles ($H_2O$, $CH_4$), thereby channeling the reaction flux selectively to C–N coupling for efficient methane amination.

## 4 Conclusions

In summary, we have elucidated the electrochemical methane amination mechanism on graphene-supported $IrN_4$ single-atom sites using constant-potential GCE-DFT calculations combined with electronic structure and kinetic analyses. Under alkaline anodic conditions, the $IrN_4$ center undergoes potential-induced coordination evolution to form a bis-axial $*CH_2$–$*NH_2$ resting state. This evolution is driven by selective axial ligation: Initial PCET favors $*CH_3$ over $*NH_2$ and *OH due to reduced Pauli repulsion, followed by $*NH_2$ coordination enabled by σ–π synergy and trans-axial electronic cooperativity. The resulting *pseudo*-octahedral environment suppresses OER by excluding *OH adsorption while stabilizing a reactive, electrophilic $*CH_2$ carbene protected against deep dehydrogenation to *CH. Kinetic studies, supported by the ASM-based analysis, demonstrate that this intermediate selectively promotes concerted C–N coupling with $NH_3$, outperforming C–C and C–O pathways due to superior frontier orbital matching and donor–acceptor interactions. Overall, this study demonstrates how applied potential can dynamically tune the axial coordination of SACs, effectively shifting the reactive center from the metal atom to the axially coordinated ligand. This provides a novel conceptual framework for designing electrocatalysts that achieve high chemoselectivity in hydrocarbon activation and sustainable C–N bond formation.

**Electronic Supplementary Material**: Supplementary material (detailed reaction pathways, crystal orbital Hamilton population (COHP) analyses, and coordinates of the relevant structures) is available in the online version of this article at https://doi.org/10.26599/NR.2026.94908484.

## Data availability

All data needed to support the conclusions in the paper are presented in the manuscript and the ESM. Additional data related to this paper may be requested from the corresponding author upon request.

## Acknowledgements

This work was supported by China Postdoctoral Science Foundation (No. 2025M780972), the National Natural Science Foundation of China (No. 22525302), the NSFC Center for Single-Atom Catalysis (No. 22388102), and the National Key Research and Development Program of China (No. 2022YFA1503000). We are grateful to the Center of High-Performance Computing at Tsinghua University for providing computational resources.

## Declaration of competing interest

All the contributing authors report no conflict of interests in this work.

## Author contribution statement

W. Y. L.: Conceptualization, investigation, data curation, writing – original draft. Z. Y. W.: Conceptualization. J. L.: Supervision, funding acquisition. H. X.: Conceptualization, supervision, funding acquisition, writing – review & editing.

## Use of AI statement

None.

## References

[1] Lelieveld, J.; Lechtenböhmer, S.; Assonov, S. S.; Brenninkmeijer, C. A. M.; Dienst, C.; Fischedick, M.; Hanke, T. Low methane leakage from gas pipelines. *Nature* **2005**, *434*, 841–842.

[2] Hartwig, J. F. Evolution of C–H bond functionalization from methane to methodology. *J. Am. Chem. Soc.* **2016**, *138*, 2–24.

[3] Song, H.; Meng, X. G.; Wang, Z.-J.; Liu, H. M.; Ye, J. H. Solar-energy-mediated methane conversion. *Joule* **2019**, *3*, 1606–1636.

[4] Meng, X. G.; Cui, X. J.; Rajan, N. P.; Yu, L.; Deng, D. H.; Bao, X. H. Direct methane conversion under mild condition by thermo-, electro-, or photocatalysis. *Chem* **2019**, *5*, 2296–2325.

[5] Tang, P.; Zhu, Q. J.; Wu, Z. X.; Ma, D. Methane activation: The past and future. *Energy Environ. Sci.* **2014**, *7*, 2580–2591.

[6] Jang, E. J.; Lee, J.; Oh, D. G.; Kwak, J. H. $CH_4$ oxidation activity in Pd and Pt–Pd bimetallic catalysts: Correlation with surface $PdO_x$ quantified from the DRIFTS study. *ACS Catal.* **2021**, *11*, 5894–5905.

[7] Lustemberg, P. G.; Mao, Z. T.; Salcedo, A.; Irigoyen, B.; Ganduglia-Pirovano, M. V.; Campbell, C. T. Nature of the active sites on Ni/$CeO_2$ catalysts for methane conversions. *ACS Catal.* **2021**, *11*, 10604–10613.

[8] Yan, L. H.; Jiang, L. L.; Qian, C.; Zhou, S. D. Electrocatalytic conversion of methane: Recent progress and future prospects. *Energy Rev.* **2024**, *3*, 100065.

[9] Xie, S. J.; Lin, S. Q.; Zhang, Q. H.; Tian, Z. Q.; Wang, Y. Selective electrocatalytic conversion of methane to fuels and chemicals. *J. Energy Chem.* **2018**, *27*, 1629–1636.

[10] Yuliati, L.; Yoshida, H. Photocatalytic conversion of methane. *Chem. Soc. Rev.* **2008**, *37*, 1592–1602.

[11] Mehmood, A.; Chae, S. Y.; Park, E. D. Low-temperature electrochemical oxidation of methane into alcohols. *Catalysts* **2024**, *14*, 58.

[12] Guo, Y. G.; Liu, T. F.; Xu, M. G.; Zhang, S. W.; Zhang, X. M.; Zhao, B. T.; Zhang, L. J.; Zhao, L.; Pan, Y.; Song, Y. F. et al. Electrochemical conversion of methane to $C_{2+}$ hydrocarbons and hydrogen. *Angew. Chem., Int. Ed.* **2025**, *64*, e202512935.

[13] Song, Q.; Xu, W. P.; Zeng, X.; Zhang, T. Q.; Hong, J.; Cullen, P. J. Electrochemical oxidation of methane to methylamine. *J. Am. Chem. Soc.* **2025**, *147*, 14966–14971.

[14] Choi, Y.; Ha, H.; Kim, J.; Seo, H. G.; Choi, H.; Jeong, B.; Yoo, J.; Crumlin, E. J.; Henkelman, G.; Kim, H. Y. et al. Unveiling direct electrochemical oxidation of methane at the ceria/gas interface. *Adv. Mater.* **2024**, *36*, 2403626.

[15] Boyd, M. J.; Latimer, A. A.; Dickens, C. F.; Nielander, A. C.; Hahn, C.; Nørskov, J. K.; Higgins, D. C.; Jaramillo, T. F. Electro-oxidation of methane on platinum under ambient conditions. *ACS Catal.* **2019**, *9*, 7578–7587.

[16] Li, J. L.; Yao, L. B.; Wu, D. Z.; King, J.; Chuang, S. S. C.; Liu, B.; Peng, Z. M. Electrocatalytic methane oxidation to ethanol on iron-nickel hydroxide nanosheets. *Appl. Catal. B: Environ.* **2022**, *316*, 121657.

[17] Stoukides, M. Electrochemical studies of methane activation. *J. Appl. Electrochem.* **1995**, *25*, 899–912.

[18] Lv, L. Y.; Tan, H.; Kong, Y.; Tang, B.; Ji, Q. Q.; Liu, Y. Y.; Wang, C.; Zhuang, Z. C.; Wang, H. J.; Ge, M. et al. Breaking the scaling relationship in C–N coupling via the doping effects for efficient urea electrosynthesis. *Angew. Chem., Int. Ed.* **2024**, *63*, e202401943.

[19] Cheng, M. Y.; Wang, S.; Dai, Z. C.; Xia, J.; Zhang, B. C.; Feng, P. Y.; Zhu, Y.; Zhang, Y. Y.; Zhang, G. Q. Rectifying heterointerface facilitated C–N coupling dynamics enables efficient urea electrosynthesis under ultralow potentials. *Angew. Chem., Int. Ed.* **2025**, *64*, e202413534.

[20] Li, Q. Y.; Liu, J. J.; Wu, Z.; Deng, A. M.; Liu, J. N.; Chen, T.; Wei, J. L.; Zhang, Y. Q.; Liu, H. W. Recent advances in electrocatalytic C–N coupling for urea synthesis. *ChemSusChem* **2025**, *18*, e202401865.

[21] Liu, J. C.; Luo, F.; Li, J. Electrochemical potential-driven shift of frontier orbitals in M–N–C single-atom catalysts leading to inverted adsorption energies. *J. Am. Chem. Soc.* **2023**, *145*, 25264–25273.

[22] Qiu, Y. Z.; Liu, X. M.; Li, W. Y.; Li, J.; Xiao, H. Transient dangling active sites of Fe(III)–N–C single-atom catalyst for efficient electrochemical $CO_2$ reduction reaction. *Angew. Chem., Int. Ed.* **2025**, *64*, e202424150.

[23] Qiao, B. T.; Wang, A. Q.; Yang, X. F.; Allard, L. F.; Jiang, Z.; Cui, Y. T.; Liu, J. Y.; Li, J.; Zhang, T. Single-atom catalysis of CO oxidation using $Pt_1/FeO_x$. *Nat. Chem.* **2011**, *3*, 634–641.

[24] Yang, X. F.; Wang, A. Q.; Qiao, B. T.; Li, J.; Liu, J. Y.; Zhang, T. Single-atom catalysts: A new frontier in heterogeneous catalysis. *Acc. Chem. Res.* **2013**, *46*, 1740–1748.

[25] Wang, A. Q.; Li, J.; Zhang, T. Heterogeneous single-atom catalysis. *Nat. Rev. Chem.* **2018**, *2*, 65–81.

[26] Liu, J. C.; Tang, Y.; Wang, Y. G.; Zhang, T.; Li, J. Theoretical understanding of the stability of single-atom catalysts. *Natl. Sci. Rev.* **2018**, *5*, 638–641.

[27] Zhuo, H. Y.; Zhang, X.; Liang, J. X.; Yu, Q.; Xiao, H.; Li, J. Theoretical understandings of graphene-based metal single-atom catalysts: Stability and catalytic performance. *Chem. Rev.* **2020**, *120*, 12315–12341.

[28] Xu, T. Z.; Wang, Z. F.; Liu, T. Y.; Wang, F. F.; Jing, Y. Mechanistic insights into methylamine electrosynthesis from $CO_2$ and NO on Co-based dual-atom catalysts. *J. Am. Chem. Soc.* **2025**, *147*, 26969–26979.

[29] Ma, D. W.; Zeng, Z. P.; Liu, L. L.; Jia, Y. Theoretical screening of the transition metal heteronuclear dimer anchored graphdiyne for electrocatalytic nitrogen reduction. *J. Energy Chem.* **2021**, *54*, 501–509.

[30] Li, Z.; Chen, Y. J.; Ji, S. F.; Tang, Y.; Chen, W. X.; Li, A.; Zhao, J.; Xiong, Y.; Wu, Y. E.; Gong, Y. et al. Iridium single-atom catalyst on nitrogen-doped carbon for formic acid oxidation synthesized using a general host–guest strategy. *Nat. Chem.* **2020**, *12*, 764–772.

[31] Wang, J. H.; Bai, J. D.; Cang, Y. Q.; Li, Q.; Fan, X.; Lin, H. P. Noble metal single-atom coordinated to nitrogen, oxygen, and carbon as electrocatalysts for oxygen evolution. *Catalysts* **2023**, *13*, 1378.

[32] Wang, J.; Zheng, M. Y.; Zhao, X.; Fan, W. L. Structure-performance descriptors and the role of the axial oxygen atom on M–$N_4$–C single-atom catalysts for electrochemical $CO_2$ reduction. *ACS Catal.* **2022**, *12*, 5441–5454.

[33] Kumar, P.; Al-Attas, T. A.; Hu, J. G.; Kibria, M. G. Single atom catalysts for selective methane oxidation to oxygenates. *ACS Nano.* **2022**, *16*, 8557–8618.

[34] Melander, M. M. Grand canonical ensemble approach to electrochemical thermodynamics, kinetics, and model Hamiltonians. *Curr. Opin. Electrochem.* **2021**, *29*, 100749.

[35] Melander, M. M. Grand canonical rate theory for electrochemical and electrocatalytic systems I: General formulation and proton-coupled electron transfer reactions. *J. Electrochem. Soc.* **2020**, *167*, 116518.

[36] Melander, M.; Kuisma, M.; Christensen, T.; Honkala, K. Grand-canonical approach to density functional theory of electrocatalytic systems: Thermodynamics of solid-liquid interfaces at constant ion and electrode potentials. *J. Chem. Phys.* **2018**, *150*, 041706.

[37] Xia, Z. M.; Xiao, H. Grand canonical ensemble modeling of electrochemical interfaces made simple. *J. Chem. Theory Comput.* **2023**, *19*, 5168–5175.

[38] Kresse, G.; Hafner, J. *Ab initio* molecular dynamics for liquid metals. *Phys. Rev. B* **1993**, *47*, 558–561.

[39] Kresse, G.; Furthmüller, J. Efficient iterative schemes for *ab initio* total-energy calculations using a plane-wave basis set. *Phys. Rev. B* **1996**, *54*, 11169–11186.

[40] Kresse, G.; Furthmüller, J. Efficiency of *ab-initio* total energy calculations for metals and semiconductors using a plane-wave basis set. *Comput. Mater. Sci.* **1996**, *6*, 15–50.

[41] Perdew, J. P.; Burke, K.; Ernzerhof, M. Generalized gradient approximation made simple. *Phys. Rev. Lett.* **1996**, *77*, 3865–3868.
[42] Blöchl, P. E. Projector augmented-wave method. *Phys. Rev. B* **1994**, *50*, 17953–17979.
[43] Kresse, G.; Joubert, D. From ultrasoft pseudopotentials to the projector augmented-wave method. *Phys. Rev. B* **1999**, *59*, 1758–1775.
[44] Monkhorst, H. J.; Pack, J. D. Special points for Brillouin-zone integrations. *Phys. Rev. B* **1976**, *13*, 5188–5192.
[45] Henkelman, G.; Jónsson, H. A dimer method for finding saddle points on high dimensional potential surfaces using only first derivatives. *J. Chem. Phys.* **1999**, *111*, 7010–7022.
[46] Heyden, A.; Bell, A. T.; Keil, F. J. Efficient methods for finding transition states in chemical reactions: Comparison of improved dimer method and partitioned rational function optimization method. *J. Chem. Phys.* **2005**, *123*, 224101.
[47] Sundararaman, R.; Goddard, W. A.; Arias, T. A. Grand canonical electronic density-functional theory: Algorithms and applications to electrochemistry. *J. Chem. Phys.* **2017**, *146*, 114104.
[48] Islam, S. M. R.; Khezeli, F.; Ringe, S.; Plaisance, C. An implicit electrolyte model for plane wave density functional theory exhibiting nonlinear response and a nonlocal cavity definition. *J. Chem. Phys.* **2023**, *159*, 234117.
[49] Liu, L. Y.; Xiao, H. Inverted region in electrochemical reduction of $CO_2$ induced by potential-dependent Pauli repulsion. *J. Am. Chem. Soc.* **2023**, *145*, 14267–14275.
[50] Wang, Z. Y.; Xiao, H. Fleeting-active-site-thrust oxygen evolution reaction by iron cations from the electrolyte. *J. Am. Chem. Soc.* **2024**, *146*, 29540–29550.
[51] Raupach, M.; Tonner, R. A periodic energy decomposition analysis method for the investigation of chemical bonding in extended systems. *J. Chem. Phys.* **2015**, *142*, 194105.
[52] Ziegler, T.; Rauk, A. On the calculation of bonding energies by the Hartree Fock Slater method. *Theor. Chim. Acta* **1977**, *46*, 1–10.
[53] te Velde, G.; Baerends, E. J. Precise density-functional method for periodic structures. *Phys. Rev. B* **1991**, *44*, 7888–7903.
[54] *Amsterdam Modeling Suite*, AMS2022.103; SCM: The Netherlands, 2022.
[55] Fernández, I.; Bickelhaupt, F. M. The activation strain model and molecular orbital theory: Understanding and designing chemical reactions. *Chem. Soc. Rev.* **2014**, *43*, 4953–4967.